

Observation of an unpaired photonic Dirac point

Gui-Geng Liu^{1,#}, Peiheng Zhou^{2,#}, Yihao Yang^{1,3,*}, Haoran Xue¹, Xin Ren², Xiao Lin¹,

Hong-xiang Sun⁴, Lei Bi², Yidong Chong^{1,3,*}, and Baile Zhang^{1,3,*}

¹Division of Physics and Applied Physics, School of Physical and Mathematical Sciences, Nanyang Technological University, 21 Nanyang Link, Singapore 637371, Singapore.

²National Engineering Research Center of Electromagnetic Radiation Control Materials, State Key Laboratory of Electronic Thin Film and Integrated Devices, University of Electronic Science and Technology of China, Chengdu 610054, China.

³Centre for Disruptive Photonic Technologies, The Photonics Institute, Nanyang Technological University, 50 Nanyang Avenue, Singapore 639798, Singapore.

⁴Research Center of Fluid Machinery Engineering and Technology, Faculty of Science, Jiangsu University, Zhenjiang, China.

These authors contributed equally to this work.

*yang.yihao@ntu.edu.sg (Y.Y.); yidong@ntu.edu.sg (Y.C.); blzhang@ntu.edu.sg (B.Z.)

Abstract

At photonic Dirac points, electromagnetic waves are governed by the same equations as two-component massless relativistic fermions. However, photonic Dirac points are known to occur in pairs in “photonic graphene” and other similar photonic crystals, which necessitates special precautions to excite only states near one of the Dirac points. Systems hosting unpaired photonic Dirac points are significantly harder to realize, as they require broken time-reversal symmetry. Here, we report on the first observation of an unpaired Dirac point in a planar two-dimensional photonic crystal. The structure incorporates gyromagnetic materials, which break time-reversal symmetry; the unpaired Dirac point occurs when a parity-breaking parameter is fine-tuned to a topological transition between a photonic Chern insulator and a conventional photonic insulator phase. Evidence for the unpaired Dirac point is provided by transmission and field-mapping experiments, including a demonstration of strongly non-reciprocal reflection. This photonic crystal is suitable for investigating the unique features of two-dimensional Dirac states, such as one-way Klein tunneling.

Introduction

In a two-dimensional (2D) bandstructure, the linear intersection of two bands at a single point in momentum space is called a Dirac point. Near such a point, the Bloch waves are governed by the same Dirac Hamiltonian that describes a two-component massless relativistic fermion¹⁻³. It is well known that the bandstructure of the 2D material graphene¹⁻³ possesses Dirac points at the two inequivalent corners of its hexagonal Brillouin zone (BZ), and similar pairs of Dirac points have been realized in optical lattices⁴⁻⁶ as well as classical acoustic⁷⁻⁹, photonic¹⁰⁻¹⁵, and plasmonic^{16, 17} structures. In 2D systems preserving time-reversal symmetry (T), Dirac points necessarily occur in pairs¹⁸. The simultaneous existence of two Dirac cones, or “valleys”, implies that in order to probe features of 2D Dirac particles (e.g., pseudo-diffusion^{19, 20}, Klein tunneling²¹⁻²³, and Zitterbewegung^{24, 25}), special precautions must be taken to ensure that only one valley is ever excited. Depending on the system geometry, this is not always possible, because defects and interfaces can give rise to strong inter-valley scattering.

On the other hand, it is known that certain bandstructures can exhibit unpaired Dirac points. For instance, the surface states of three-dimensional (3D) strong topological insulators exhibit unpaired Dirac points on each surface²⁶⁻²⁸; this has been observed in condensed-matter systems²⁹ but has never been experimentally achieved in a classical-wave system such as a photonic crystal (PhC). Another method is exemplified theoretically by the famous Haldane model in a 2D honeycomb lattice, where an unpaired Dirac point appears during a topological transition between the conventional insulator and Chern insulator phases³⁰. Notably, this requires time-reversal symmetry (T) to be broken at the transition point (the sign of the T -breaking determines which BZ corner the Dirac point occurs at). Following the idea of breaking T , unpaired Dirac points can also arise in Floquet systems, which are driven periodically in time³¹. Floquet systems have been experimentally simulated using 3D photonic structures of coupled waveguides³²⁻³⁶, and a single Dirac cone has been demonstrated to exist in the “quasienergy” spectrum (where on-axis momentum plays the role of energy)³⁴. However, phenomena such as one-way Klein tunneling are challenging to observe in that platform, due to small system sizes, lack of frequency selectivity, and other technical limitations. To our knowledge, there is no previous realization of an unpaired Dirac point in the energy (rather than quasienergy) bandstructure of a 2D classical-wave system.

Here, we report on the experimental observation of an unpaired photonic Dirac point in a 2D

PhC operating at microwave frequencies. T symmetry is broken by using gyromagnetic materials biased by an external magnetic field. The PhC is fine-tuned by varying the orientation of three dielectric scatterers in each unit cell, which controls the magnitude of parity (P) symmetry breaking. At a specific orientation angle, an unpaired Dirac point appears between the second and third transverse-magnetic (TM) polarized bands, at a corner of the hexagonal Brillouin zone. This is the transition point between a Chern insulator phase (with nonzero Chern numbers) and a topologically trivial insulator phase (with zero Chern numbers). This set of features is similar to the theoretical Haldane model in the T -broken regime (nonzero Haldane flux)^{30,37,38}. Transmission measurements reveal that the closing and re-opening of the band gaps occur at the orientation angle predicted by numerical calculations. Using direct field mapping, we show that an unpolarized point source excites Bloch states in a single valley, centered on one of the two inequivalent BZ corners. Finally, we demonstrate the phenomenon of non-reciprocal reflection, where microwave beams incident from different directions outside the PhC is selectively reflected, depending on the availability of an unpaired Dirac point within the PhC to couple to. The realization of an unpaired photonic Dirac point in a PhC setting opens up many other possibilities for exploring the behavior and applications of 2D Dirac modes, including one-way Klein tunneling³⁹, weak antilocalization^{31,40}, and enhancement of magneto-optical activity by near-zero effective refractive indices⁴¹.

Results

The PhC, depicted in Fig. 1(a), consists of a 2D triangular lattice with lattice constant $a=17.5$ mm. Each unit cell comprises a gyromagnetic cylinder surrounded by three right-triangular dielectric pillars (see Methods for the material parameters). The PhC is placed in an air-loaded parallel-plate waveguide (see Methods; in the photograph in Fig. 1(a), the top plate has been removed for visualization). The orientation of the three dielectric pillars is characterized by an angle θ , which is used to modulate the strength of the in-plane P -breaking⁴². We study TM modes, which have E -field polarized along the cylinder axis (defined as the z -axis). For $\theta=0^\circ$ and zero biasing magnetic field, the PhC is P and T symmetric, and its bandstructure contains two Dirac points located at the K and K' points (the corners of the BZ), similar to graphene. Applying a static magnetic field $B=0.4$ Tesla along the z -axis breaks T , and hence opens a complete photonic

bandgap between the second and the third TM bands, as shown numerically in Fig. 1(b). Next, increasing θ widens the bandgap at K while narrowing the bandgap at K'. At the specific value $\theta=12.9^\circ$, the bandgap at K' closes completely to form a Dirac point at 9.01 GHz. Further increasing θ , e.g. to 30° , reopens the bandgap. Figure 1(c) plots the variation of the bandgap widths at K and K' versus θ , showing the formation of unpaired Dirac points at $\theta=-12.9^\circ$ (on K) and $\theta=12.9^\circ$ (on K').

The effective Hamiltonian governing the second and third TM bands near K (K') is

$$\hat{H} = v_D (\hat{\sigma}_x \hat{\tau}_z \delta k_x + \hat{\sigma}_y \hat{\tau}_0 \delta k_y) + \hat{\sigma}_z (\hat{\tau}_z m_T + \hat{\tau}_0 m_P), \quad (1)$$

where v_D is the group velocity around the Dirac point, δk_i is the momentum deviation from the K (K') point, $\hat{\sigma}_i$ and $\hat{\tau}_i$ are the Pauli matrices operating on orbital and valley subspaces, m_P and m_T are the effective mass induced by the breaking of P and T respectively. When m_P and m_T are both zero, Eq. (1) reduces to the massless Dirac Hamiltonian. Perturbatively breaking P and/or T generates a bandgap, whose magnitude is proportional to $|m_P + m_T|$ at K and $|m_P - m_T|$ at K'. Clearly, an unpaired Dirac point forms at K or K' when $m_P = -m_T$ or $m_P = m_T$ respectively, which correspond to orientation angles of $\theta = -12.9^\circ$ and 12.9° in the actual PhC for 0.4 Tesla applied magnetic field. The phase transition can also be achieved by adjusting the external magnetic field while keeping θ constant, which corresponds to tuning m_T (see Supplementary Note 2).

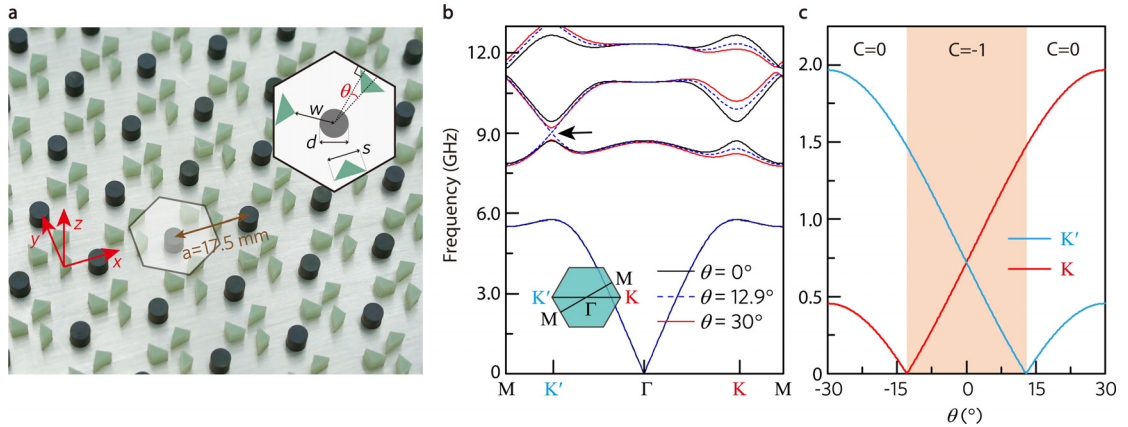


Figure 1. Reconfigurable gyromagnetic PhC exhibiting an unpaired Dirac point. (a) Photograph of the PhC sample in a parallel-plate waveguide. The spacing between the upper and lower aluminum plates is 4 mm. Inset:

schematic of a unit cell, which consists of a gyromagnetic cylinder (dark gray circle) and three dielectric right-triangular pillars (green triangles). The gyromagnetic cylinder has diameter $d=0.24a$, and the right-triangular pillars have hypotenuse widths $s=0.28a$. The distance between the unit cell center and nearest triangular vertices is $w=0.33a$. The angle θ indicates the orientation of the triangular pillars within the unit cell, relative to the three primitive vectors of the hexagonal lattice. In the depicted configuration, $\theta=12.9^\circ$. (b) PhC band structures under a 0.4 Tesla external magnetic field for $\theta=0^\circ$, 12.9° , and 30° . For at $\theta=12.9^\circ$, an unpaired Dirac point appears at K' (indicated by the black arrow). (c) Widths of the bandgap between the second and the third band at K and K' , as a function of θ . The bandgap at K' (K) closes when $\theta=12.9^\circ$ ($\theta=-12.9^\circ$). For $|\theta|<12.9^\circ$, highlighted in light orange, the bandstructure has a topologically nontrivial bandgap, with the first band having a numerically-calculated Chern number of $C = -1$ (see Supplementary Note 1).

Next, we measure the bulk and edge transmissions to characterize the bandgaps and topological properties of the PhC with different orientations of dielectric pillars in a z -oriented static magnetic field of $B=0.4$ Tesla. As shown in the first column of Fig. 2, three different domain walls are constructed between a zigzag aluminum cladding layer (acting as a trivial bandgap material) and the PhC with $\theta=0^\circ$, 12.9° , and 30° , respectively. We measure the bulk and edge transmissions with a vector network analyzer (see Methods). The edge transmissions S_{21}/S_{12} are measured when the exciting dipole antenna is placed at Port 1/Port 2, with the detecting dipole antenna at Port 2/Port 1. The bulk transmissions are measured with both source and receiver antennas placed inside the PhC, 18 cm away from each other. The first column of Fig. 2 shows the simulated field distributions when the point source is at Port 1 at 9.0 GHz, for the three cases.

The measured edge and bulk transmissions are plotted in the second column of Fig. 2. For $\theta=0^\circ$, we find that $|S_{21}|$ is approximately 30 dB larger than both $|S_{12}|$ and the bulk transmission in a frequency range around 9.0 GHz. This is consistent with the existence of a topologically nontrivial bulk bandgap with a unidirectional edge state – i.e., a photonic analogue of a Chern insulator⁴³. For $\theta=12.9^\circ$, the edge and bulk transmissions almost overlap, and no distinct gap is observed, indicating that the bulk is gapless; this corresponds to the unpaired Dirac point (the dashed blue curve in Fig. 1(b)). For $\theta=30^\circ$, both the edge and bulk transmissions are gapped around 9.0 GHz, indicating that the PhC has a topologically trivial bandgap. These experimental results are further supported by the numerically calculated band diagrams of the domain wall structures, shown in the third column of Fig. 2. Thus, by choosing the orientation of the triangle pillars in the experimental sample, we are able to precisely access the topological transition of the PhC (between Chern insulator and conventional insulator phases), where the unpaired Dirac point appears.

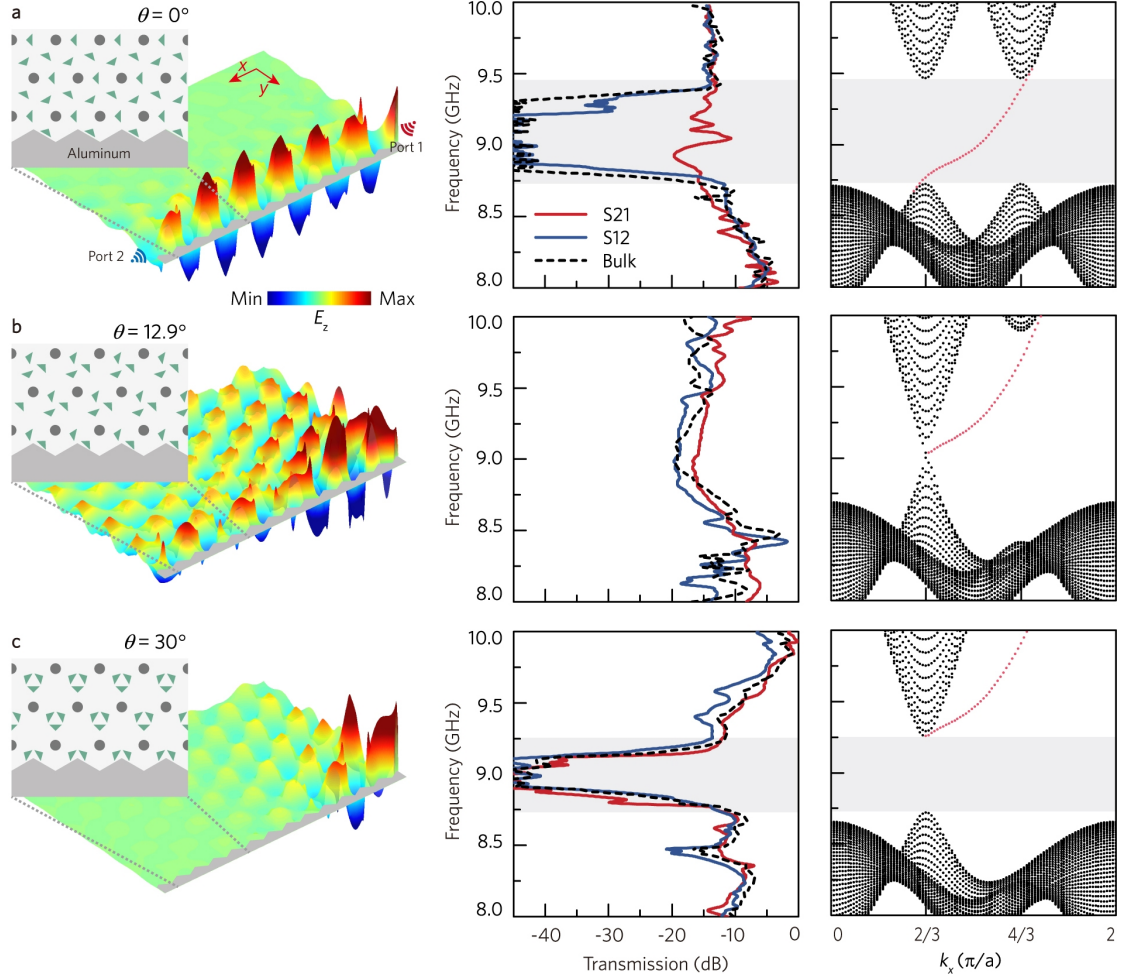


Figure 2. Observation of an unpaired Dirac point associated with a topological phase transition. The orientation angles are (a) $\theta=0^\circ$ (topologically nontrivial bandgap over 8.72~9.47 GHz), (b) $\theta=12.9^\circ$ (gapless), and (c) $\theta=30^\circ$ (topologically trivial bandgap over 8.75~9.26 GHz). The first column shows the PhC configuration, which includes a domain wall, and simulated electric field distribution excited by a 9.0 GHz source at Port 1. The second column plots the experimentally-measured normalized bulk and edge transmission (S-parameter magnitudes). The third column shows the numerically-calculated band diagrams for the structures (including domain wall); black dots represent projected bulk states, and the red dots are edge states localized along the boundary. The numerical data from the third column are used to estimate the bandgap frequencies.

An important property of this unpaired Dirac point is that it occurs at the K' point, and the bandstructure is gapped at K . Because of this, sources near the Dirac frequency only excite one valley. This is demonstrated by the experimental results shown in Fig. 3(a). Here, an unpolarized point source (labeled by a pink star) is placed inside the PhC ($\theta=12.9^\circ$ and $B=0.4$ Tesla); the sample configuration is shown schematically in the inset to Fig. 3(a). We measure the field patterns outside the PhC, which are caused by the refraction of the PhC's bulk states into the empty-waveguide region through a zigzag termination. The measured field pattern at 9.05 GHz,

along with the corresponding numerically simulated results, are plotted. We observe that a single directional beam is refracted out of the PhC into the empty-waveguide region, consistent with the fact that there is only a single valley of bulk states within the PhC. This valley is wave-matched to right-moving outgoing waves, as indicated in Figs. 3(b)-(c). For comparison, we repeat the experiment for $\theta=0^\circ$ and $B=0$ Tesla, with the results shown in Figs. 3 (d)-(f). In this case, there are two outgoing beams refracted into the empty-waveguide region (the operating frequency for this case, 9.76 GHz, lies near the frequency of the paired Dirac points).

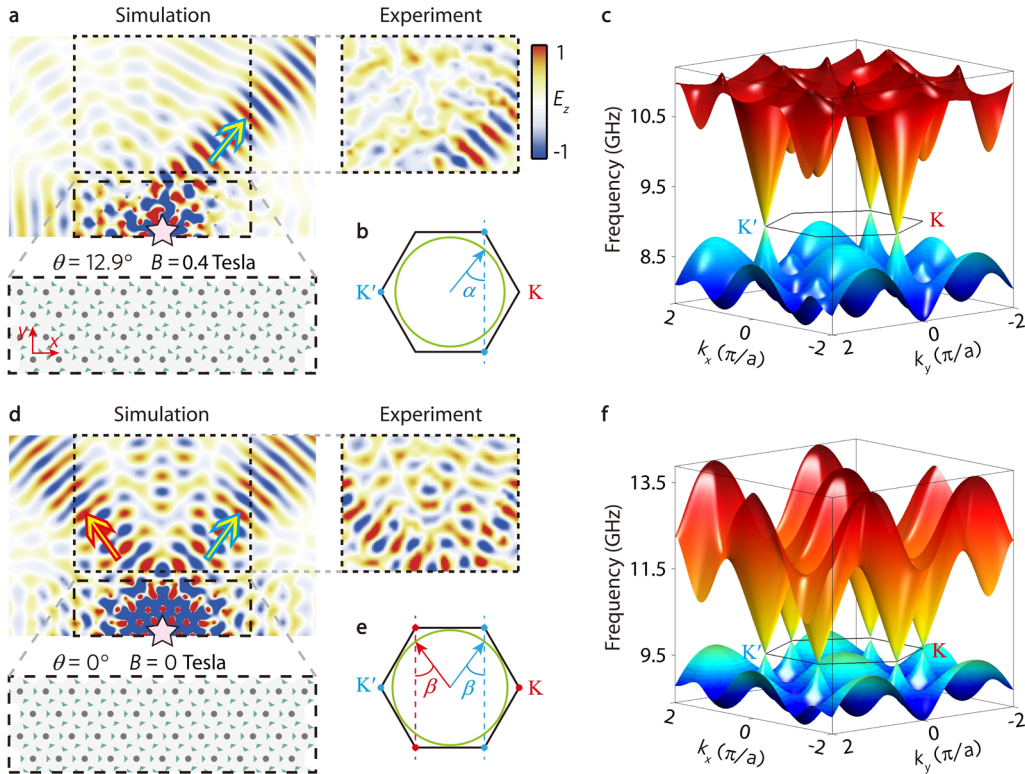


Figure 3. Refraction of unpaired and paired Dirac valleys into an empty waveguide. (a) Experimental and numerical field maps for PhC sample with $\theta=12.9^\circ$ and $B=0.4$ Tesla (whose bandstructure has an unpaired Dirac point at K'), with an upper zigzag boundary with an empty waveguide. The point source indicated by a pink star operates at 9.05 GHz. A single directional beam is emitted into the empty-waveguide region (green arrow), caused by refraction from the K' valley inside the PhC. (b) k -space analysis of how PhC valley modes outcouple. The three blue dots indicate the K' point, and the green circle is the isofrequency surface of TM empty-waveguide modes at the Dirac frequency. The resulting outcoupling angle is $\alpha=39.1^\circ$, consistent with the experimental results (c) Band structure of PhC with $\theta=12.9^\circ$ and $B=0.4$ Tesla. (d) Experimental and numerical field maps for PhC sample with $\theta=0^\circ$ and $B=0$ Tesla (whose bandstructure has Dirac points at K and K'), with point source (pink star) operating at 9.76 GHz. Two directional beams are emitted into the empty-waveguide region (red and green arrows), caused by refraction from K' and K valley states inside the PhC. (e) k -space analysis for the PhC with paired Dirac points, which yields an outcoupling angle $\beta=35.8^\circ$, consistent with experimental results. (f) 2D band structure for PhC with $\theta=0^\circ$ and $B=0$ Tesla.

Finally, we show that the unpaired Dirac point enables the phenomenon of non-reciprocal reflection. As shown in Fig. 4(a), a diverging beam is incident on the upper boundary of the PhC slab ($\theta=12.9^\circ$ and $B=0.4$ Tesla) from the upper-left empty region at 9.05 GHz (close to the Dirac frequency). The measured electric field pattern shows that reflection is suppressed at an angle of $\alpha = 39.1^\circ$; this is confirmed by numerical simulations (see the left inset of Fig. 4(a) and Supplementary Note 3). This behavior is explained by matching tangential wave-vectors along the PhC boundary, as shown in Fig. 4(b). The wave with incidence angle α (blue arrow) can couple to the single valley states at K' , whereas waves at neighboring incidence angles lie outside the Dirac cone and are therefore totally reflected. However, if a diverging beam is incident from the upper-right region, as shown in Figs. 4(c)-(d), strong reflection is observed even at an angle α , as there are no valley states at K to couple into.

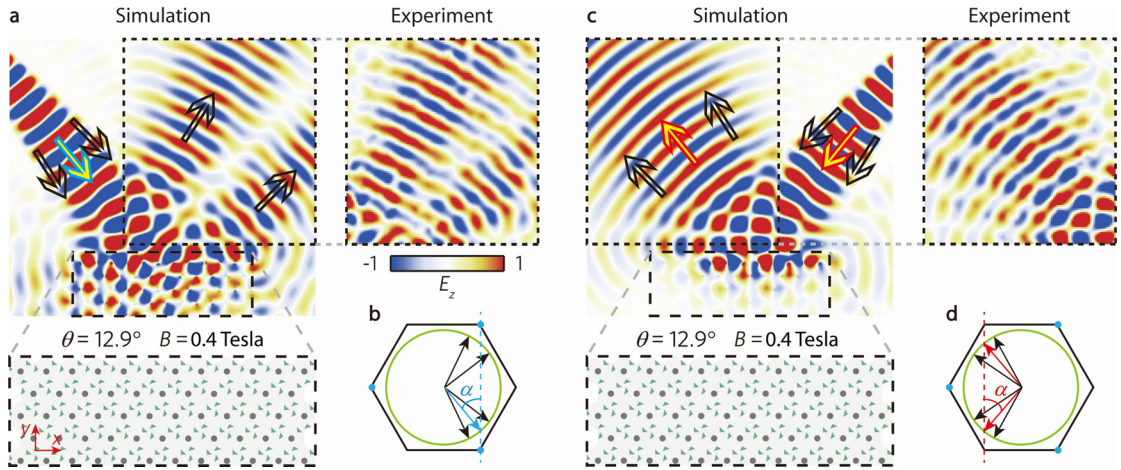


Figure 4. Non-reciprocal reflections due to the unpaired Dirac point. (a) The incident wave from the left-upper region with the approximate angle of incidence α ($=39.1^\circ$) can couple into the PhC slab ($\theta=12.9^\circ$ and $B=0.4$ Tesla). The blue arrow represents the waves with the angle of incidence α . The black arrows represent the waves with the angles of incidence deviated from α and their reflections. (b) k -space analysis on the reflection of the PhC slab of the left-upper input wave. (c) The incident wave from the right-upper region is totally reflected. The red arrows represent the wave with the angle of incidence α and its reflection. The black arrows represent the waves with the angles of incidence deviated from α and their reflections. (d) k -space analysis on the reflection of the PhC slab of the right-upper input wave.

We have thus observed the experimental signatures of an unpaired photonic Dirac point in a 2D planar gyromagnetic PhC at microwave frequencies. The unpaired Dirac point occurs at the phase transition between a topologically nontrivial Chern insulator and a topologically trivial photonic insulator, as verified by transmission measurements. We confirm the existence of valley

states at one corner of the Brillouin zone but not the other, by direct field mapping of the microwaves refracting into an empty waveguide, as well as non-reciprocal reflection from the surface of the PhC. This work opens up multiple avenues for explorations and applications of the unpaired Dirac point, including one-way Klein tunneling³⁹, implementation of magneto-optical near-zero refractive index media⁴¹, and manipulation of valley states for robust bulk transport²⁸.

Acknowledgments

We are very grateful to S. J. Ren and J. D. Wang from the Southwest Institute of Applied Magnetism (Mianyang, China) for providing the ferrite rods and electromagnet for the microwave experiments. This work was sponsored by the Singapore Ministry of Education under grant numbers MOE2018-T2-1-022 (S), MOE2015-T2-2-008, MOE2016-T3-1-006 and Tier 1 RG174/16 (S), and by National Key Research and Development Program of China under grant number 2016YFB1200100, and by the program of China Scholarships Council under grant number 201806075001, and by the National Natural Science Foundation of China under grant number 11774137.

Authors Contributions

All authors contributed extensively to this work. G.G.L., P.Z., H.X., and L.B. designed the structure and fabricated the sample. G.G.L. and P.Z. performed the simulation. G.G.L., Y.Y., P.Z., and H.X. designed the experiments. G.G.L., P.Z., and X.R. carried out the experiments. G.G.L., Y.Y., and P.Z. provided major theoretical analysis. G.G.L., H.X.S., and X.L. drew the figures. G.G.L., Y.Y., P.Z., X.L., H.X.S., Y.C., and B.Z. produced the manuscript. B.Z. and Y.C. supervised the project. All authors participated in discussions and reviewed the manuscript.

Competing Financial Interests

The authors declare no competing financial interests.

Data availability

The data that support the plots within this paper and other findings of this study are available from the corresponding author upon request.

Methods

Sample and experimental measurement. The right-triangular dielectric material used in the experiment is FR4, which has a measured relative permittivity of 4.4 and loss tangent of 0.019. The gyromagnetic material is yttrium iron garnet (YIG), a ferrite with measured relative permittivity 13.0 and loss tangent 0.0002. Its measured saturation magnetization is $M_s = 1780$ Gauss, with a gyromagnetic resonance loss width of 35 Oe. The external magnetic field is applied by a large electromagnet; the spatial non-uniformity of the magnetic field is measured to be less than 2% across the sample. Pixeled holes of diameter 1.8 mm are drilled into the top aluminum plate. To excite and measure the electric field, identically constructed antennas are inserted the holes, making contact with the bottom plate, and connected to a vector network analyzer (R&S ZNB20). Field distributions are measured by detecting the local intensity at the different holes, one by one. The samples are surrounded by microwave absorber.

Simulation. The dispersion relations and field patterns are simulated using the finite element software COMSOL Multiphysics. The bandstructures in Fig. 2 are calculated using a supercell that is 20 cells wide, with aluminum walls are modeled as a perfect electric conductor (PEC). Material losses are neglected during these simulations. The YIG rods are modeled as $\mu=\mu_0$ and $\varepsilon=13.0\varepsilon_0$ for $B=0$ Tesla. For $B=0.4$ Tesla, $\varepsilon=13.0\varepsilon_0$ and the relative magnetic permeability has the form

$$\mu=\mu_0 \begin{bmatrix} \mu_r & i\kappa & 0 \\ -i\kappa & \mu_r & 0 \\ 0 & 0 & 1 \end{bmatrix},$$

where $\mu_r=1+\frac{\omega_0\omega_m}{\omega_0^2-\omega^2}$, $\kappa=\frac{\omega\omega_m}{\omega_0^2-\omega^2}$, $\omega_m=\gamma M_s$, and $\omega_0=\gamma H_0$, where H_0 is the external magnetic field, $\gamma=1.76 \times 10^{11} \text{ s}^{-1}\text{T}^{-1}$ is the gyromagnetic ratio, and ω is the operating frequency⁴⁴. For the FR4 pillars, we take $\mu=\mu_0$ and $\varepsilon=4.4\varepsilon_0$.

References

1. Novoselov, K.S., Geim, A.K., Morozov, S., Jiang, D., Katsnelson, M.I., Grigorieva, I., Dubonos, S., Firsov & AA. Two-dimensional gas of massless Dirac fermions in graphene. *Nature* **438**, 197 (2005).
2. Zhang, Y., Tan, Y.-W., Stormer, H.L. & Kim, P. Experimental observation of the quantum Hall effect and Berry's phase in graphene. *Nature* **438**, 201 (2005).
3. Neto, A.C., Guinea, F., Peres, N.M., Novoselov, K.S. & Geim, A.K. The electronic properties of graphene. *Reviews of Modern Physics* **81**, 109 (2009).
4. Tarruell, L., Greif, D., Uehlinger, T., Jotzu, G. & Esslinger, T. Creating, moving and merging Dirac points with a Fermi gas in a tunable honeycomb lattice. *Nature* **483**, 302 (2012).
5. Polini, M., Guinea, F., Lewenstein, M., Manoharan, H.C. & Pellegrini, V. Artificial honeycomb

- lattices for electrons, atoms and photons. *Nature Nanotechnology* **8**, 625 (2013).
6. Jotzu, G., Messer, M., Desbuquois, R., Lebrat, M., Uehlinger, T., Greif, D. & Esslinger, T. Experimental realization of the topological Haldane model with ultracold fermions. *Nature* **515**, 237 (2014).
 7. Torrent, D. & Sánchez-Dehesa, J. Acoustic analogue of graphene: observation of Dirac cones in acoustic surface waves. *Physical Review Letters* **108**, 174301 (2012).
 8. Yu, S.-Y., Sun, X.-C., Ni, X., Wang, Q., Yan, X.-J., He, C., Liu, X.-P., Feng, L., Lu, M.-H. & Chen, Y.-F. Surface phononic graphene. *Nature Materials* **15**, 1243 (2016).
 9. Ma, G., Xiao, M. & Chan, C. Topological phases in acoustic and mechanical systems. *Nature Reviews Physics*, 1 (2019).
 10. Haldane, F. & Raghu, S. Possible realization of directional optical waveguides in photonic crystals with broken time-reversal symmetry. *Physical Review Letters* **100**, 013904 (2008).
 11. Huang, X., Lai, Y., Hang, Z.H., Zheng, H. & Chan, C. Dirac cones induced by accidental degeneracy in photonic crystals and zero-refractive-index materials. *Nature Materials* **10**, 582 (2011).
 12. Plotnik, Y., Rechtsman, M.C., Song, D., Heinrich, M., Zeuner, J.M., Nolte, S., Lumer, Y., Malkova, N., Xu, J. & Szameit, A. Observation of unconventional edge states in 'photonic graphene'. *Nature Materials* **13**, 57 (2014).
 13. Lu, L., Joannopoulos, J.D. & Soljačić, M. Topological photonics. *Nature Photonics* **8**, 821 (2014).
 14. Yang, Y., Gao, Z., Xue, H., Zhang, L., He, M., Yang, Z., Singh, R., Chong, Y., Zhang, B. & Chen, H. Realization of a three-dimensional photonic topological insulator. *Nature* **565**, 622 (2019).
 15. Ozawa, T., Price, H.M., Amo, A., Goldman, N., Hafezi, M., Lu, L., Rechtsman, M.C., Schuster, D., Simon, J. & Zilberberg, O. Topological photonics. *Reviews of Modern Physics* **91**, 015006 (2019).
 16. Han, D., Lai, Y., Zi, J., Zhang, Z.-Q. & Chan, C.T. Dirac spectra and edge states in honeycomb plasmonic lattices. *Physical Review Letters* **102**, 123904 (2009).
 17. Weick, G., Woollacott, C., Barnes, W.L., Hess, O. & Mariani, E. Dirac-like plasmons in honeycomb lattices of metallic nanoparticles. *Physical Review Letters* **110**, 106801 (2013).
 18. Nielsen, H.B. & Ninomiya, M. Absence of neutrinos on a lattice:(I). Proof by homotopy theory. *Nuclear Physics B* **185**, 20-40 (1981).
 19. Zhang, X. & Liu, Z. Extremal transmission and beating effect of acoustic waves in two-dimensional sonic crystals. *Physical Review Letters* **101**, 264303 (2008).
 20. Zandbergen, S.R. & de Dood, M.J. Experimental observation of strong edge effects on the pseudodiffusive transport of light in photonic graphene. *Physical Review Letters* **104**, 043903 (2010).
 21. Katsnelson, M., Novoselov, K. & Geim, A. Chiral tunnelling and the Klein paradox in graphene. *Nature Physics* **2**, 620 (2006).
 22. Beenakker, C. Colloquium: Andreev reflection and Klein tunneling in graphene. *Reviews of Modern Physics* **80**, 1337 (2008).
 23. Stander, N., Huard, B. & Goldhaber-Gordon, D. Evidence for Klein tunneling in graphene p–n junctions. *Physical Review Letters* **102**, 026807 (2009).
 24. Zhang, X. Observing Zitterbewegung for photons near the Dirac point of a two-dimensional photonic crystal. *Physical Review Letters* **100**, 113903 (2008).

25. Dreisow, F., Heinrich, M., Keil, R., Tünnermann, A., Nolte, S., Longhi, S. & Szameit, A. Classical simulation of relativistic Zitterbewegung in photonic lattices. *Physical Review Letters* **105**, 143902 (2010).
26. Zhang, H., Liu, C.-X., Qi, X.-L., Dai, X., Fang, Z. & Zhang, S.-C. Topological insulators in Bi₂Se₃, Bi₂Te₃ and Sb₂Te₃ with a single Dirac cone on the surface. *Nature Physics* **5**, 438 (2009).
27. Xia, Y., Qian, D., Hsieh, D., Wray, L., Pal, A., Lin, H., Bansil, A., Grauer, D., Hor, Y.S. & Cava, R.J. Observation of a large-gap topological-insulator class with a single Dirac cone on the surface. *Nature Physics* **5**, 398 (2009).
28. Lu, L., Fang, C., Fu, L., Johnson, S.G., Joannopoulos, J.D. & Soljačić, M. Symmetry-protected topological photonic crystal in three dimensions. *Nature Physics* **12**, 337 (2016).
29. Chen, Y.L., Analytis, J.G., Chu, J.-H., Liu, Z.K., Mo, S.-K., Qi, X.L., Zhang, H.J., Lu, D.H., Dai, X., Fang, Z., Zhang, S.C., Fisher, I.R., Hussain, Z. & Shen, Z.-X. Experimental Realization of a Three-Dimensional Topological Insulator, Bi₂Te₃. *Science* **325**, 178-181 (2009).
30. Haldane, F.D.M. Model for a quantum Hall effect without Landau levels: Condensed-matter realization of the "parity anomaly". *Physical Review Letters* **61**, 2015 (1988).
31. Leykam, D., Rechtsman, M.C. & Chong, Y. Anomalous topological phases and unpaired Dirac cones in photonic Floquet topological insulators. *Physical Review Letters* **117**, 013902 (2016).
32. Rechtsman, M.C., Zeuner, J.M., Plotnik, Y., Lumer, Y., Podolsky, D., Dreisow, F., Nolte, S., Segev, M. & Szameit, A. Photonic Floquet topological insulators. *Nature* **496**, 196 (2013).
33. Gao, F., Gao, Z., Shi, X., Yang, Z., Lin, X., Xu, H., Joannopoulos, J.D., Soljačić, M., Chen, H. & Lu, L. Probing topological protection using a designer surface plasmon structure. *Nature Communications* **7**, 11619 (2016).
34. Noh, J., Huang, S., Leykam, D., Chong, Y.D., Chen, K.P. & Rechtsman, M.C. Experimental observation of optical Weyl points and Fermi arc-like surface states. *Nature Physics* **13**, 611 (2017).
35. Maczewsky, L.J., Zeuner, J.M., Nolte, S. & Szameit, A. Observation of photonic anomalous Floquet topological insulators. *Nature Communications* **8**, 13756 (2017).
36. Mukherjee, S., Spracklen, A., Valiente, M., Andersson, E., Öhberg, P., Goldman, N. & Thomson, R.R. Experimental observation of anomalous topological edge modes in a slowly driven photonic lattice. *Nature Communications* **8**, 13918 (2017).
37. Leykam, D., Mittal, S., Hafezi, M. & Chong, Y.D. Reconfigurable topological phases in next-nearest-neighbor coupled resonator lattices. *Physical Review Letters* **121**, 023901 (2018).
38. Mittal, S., Orre, V.V., Leykam, D., Chong, Y.D. & Hafezi, M. Photonic Anomalous Quantum Hall Effect. *Physical Review Letters* **123**, 043201 (2019).
39. Ni, X., Purtseladze, D., Smirnova, D.A., Slobozhanyuk, A., Alù, A. & Khanikaev, A.B. Spin-and valley-polarized one-way Klein tunneling in photonic topological insulators. *Science Advances* **4**, eaap8802 (2018).
40. Bergmann, G. Weak anti-localization—an experimental proof for the destructive interference of rotated spin 12. *Solid State Communications* **42**, 815-817 (1982).
41. Zhou, X., Leykam, D., Chattopadhyay, U., Khanikaev, A. & Chong, Y.D. Realization of a magneto-optical near-zero index medium by an unpaired Dirac point. *Physical Review B* **98**, 205115 (2018).
42. Ma, T. & Shvets, G. Scattering-free edge states between heterogeneous photonic topological

- insulators. *Physical Review B* **95**, 165102 (2017).
43. Wang, Z., Chong, Y., Joannopoulos, J.D. & Soljačić, M. Observation of unidirectional backscattering-immune topological electromagnetic states. *Nature* **461**, 772 (2009).
 44. Pozar, D.M. Microwave engineering. *Wiley* (2012).